Unexpected trapping of particles at a T junction

Daniele Vigolo[a,1,2], Stefan Radl[b], and Howard A. Stone[a,2]

[a]Department of Mechanical and Aerospace Engineering, Princeton University, Princeton, NJ 08544; and [b]Institute for Process and Particle Engineering, Graz University of Technology, 8010 Graz, Austria

Edited* by Andreas Acrivos, City College of the City University of New York, New York, NY, and approved February 20, 2014 (received for review November 20, 2013)

A common element in physiological flow networks, as well as most domestic and industrial piping systems, is a T junction that splits the flow into two nearly symmetric streams. It is reasonable to assume that any particles suspended in a fluid that enters the bifurcation will leave it with the fluid. Here we report experimental evidence and a theoretical description of a trapping mechanism for low-density particles in steady and pulsatile flows through T-shaped junctions. This mechanism induces accumulation of particles, which can form stable chains, or give rise to significant growth of bubbles due to coalescence. In particular, low-density material dispersed in the continuous phase fluid interacts with a vortical flow that develops at the T junction. As a result suspended particles can enter the vortices and, for a wide range of common flow conditions, the particles do not leave the bifurcation. Via 3D numerical simulations and a model of the two-phase flow we predict the location of particle accumulation, which is in excellent agreement with experimental data. We identify experimentally, as well as confirm by numerical simulations and a simple force balance, that there is a wide parameter space in which this phenomenon occurs. The trapping effect is expected to be important for the design of particle separation and fractionation devices, as well as used for better understanding of system failures in piping networks relevant to industry and physiology.

fluid dynamics | bubble trapping | vortex breakdown | 3D simulations

Bifurcations are found in all fluid distribution networks (Fig. 1), e.g., blood flow in the cardiovascular system (1) (Fig. 1*A*), fittings for small piping networks (Fig. 1*B*), and as elements of larger systems (2, 3) (Fig. 1*C*). Also, bifurcations are the key element in flow devices for mixing (4), heat exchange (5), and droplet formation (6). Whereas these devices have been studied in great detail, much less is known about the trajectories of suspended particles (being either solid or fluid) that enter a bifurcation. The trajectories of solid particles moving through a bifurcation, or curved channels, are of central importance for many applications, e.g., bioanalytics, particle size measurement devices (7–9), or novel membraneless filtration devices (10). In addition, examples where the trajectories of low-density particles (e.g., air bubbles) are important are found in hemodynamics, e.g., gas embolisms (1, 11, 12), which refer to air pockets trapped in blood vessels, and medical diagnostics (13, 14). Also, common industrial products contain low-density particles, e.g., paint (2) or polymers (3), and hence the prediction of the flow behavior depends on understanding the distribution of the suspended particles.

In this paper we provide a more systematic understanding of how particles move through a simple bifurcation, i.e., a T junction. From a naive point of view, a T junction distributes the incoming fluid to subsystems of a network, and particles dispersed in the fluid should be similarly distributed. This is correct only for some specific conditions. For example, small particles with a density comparable to that of the fluid tend to follow the flow and can be used as tracers in flow measurements (15). Particles having a higher density than that of the carrier fluid can cross the streamlines and eventually collide with walls (16); nonetheless the particles leave the junction. In contrast, and surprisingly, we find that under typical flow conditions, i.e., for mean flow Reynolds numbers above *ca.* 200, low-density particles will not necessarily move through the T junction, but instead will be trapped for extremely long times (Fig. 1*D*). Low-density particles and bubbles interact with the 3D flow structures at the T junction, get trapped, and accumulate. We find that this trapping is solely caused by the density difference between the two phases and the velocity and pressure distributions in these flow structures, which consist of two counterrotating vortices—buoyancy effects and lift forces familiar in other hydrodynamic two-phase systems are irrelevant. This differentiates the trapping phenomenon observed by us from previous observations of pressure-gradient-induced trapping of bubbles in vortices (17–20). Moreover, we find that the trapping can be temporary, in which case the particles get trapped but subsequently leave the T junction, or permanent, i.e., particles get trapped for infinitely long times. Because our observations depend on the density difference between the particles and the fluid, and vary systematically with Reynolds number, our findings are distinct from the kinematic separation phenomena studied in other vortical flows (21–23). To the best of our knowledge, and despite the wide range of studies of flow systems with suspended particles (engineering, medicine, etc.), there are no previous reports in the literature of such an anomalous behavior and trapping of low-density particles when traveling through a bifurcation or the T-shaped junction as we document in this paper.

Setup

To study flow through a bifurcation we realized different T-junction devices with a square cross-section and lateral size (L) between 0.4 and 4.8 mm (Fig. 1*E*) and we generated gas bubbles by electrolysis (see *Materials and Methods* for more details). The flows are characterized by the Reynolds number $Re = \rho_f UL/\mu$, where U is the (volume-averaged) mean flow speed entering the

Significance

Most flow systems we encounter in everyday life, such as cardiovascular blood flow in our body or the flow in typical domestic or industrial piping systems, present T junctions that split the flow into two streams. Another characteristic that these systems often have in common is the presence of a dispersed phase made of low-density particles or air bubbles. In this paper we present evidence that in these situations particles can get trapped at the junction, accumulate, and ultimately change the flow distribution. The unanticipated trapping mechanism can affect health and diagnostics in human beings or create malfunctions, and consequently unexpected dangers, in industrial environments. Nonetheless, the same effect can also be exploited to design new particle separation devices.

Author contributions: D.V. and H.A.S. designed research; D.V. and S.R. performed research; D.V., S.R., and H.A.S. analyzed data; and D.V., S.R., and H.A.S. wrote the paper.

The authors declare no conflict of interest.

*This Direct Submission article had a prearranged editor.

[1]Present address: Department of Chemistry and Applied Biosciences, Eidgenössische Technische Hochschule Zürich, 8093 Zurich, Switzerland.

[2]To whom correspondence may be addressed. E-mail: daniele.vigolo@chem.ethz.ch or hastone@princeton.edu.

This article contains supporting information online at www.pnas.org/lookup/suppl/doi:10.1073/pnas.1321585111/-/DCSupplemental.

www.pnas.org/cgi/doi/10.1073/pnas.1321585111

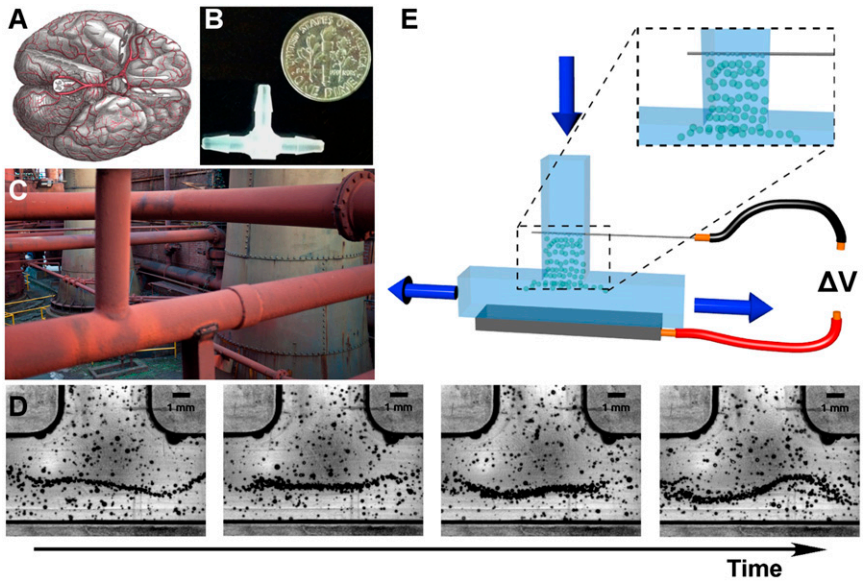

Fig. 1. T junctions and the trapping of air bubbles. T-junction geometry is common in (*A*) physiological flow systems [e.g., arteries in the brain (http://commons.wikimedia.org/wiki/File%3AGray516.png)], (*B*) small-scale tube fittings, and (*C*) industrial piping systems (http://commons.wikimedia.org/wiki/File%3ABlast_Furnace_Pipes_(5375076095).jpg). (*D*) Time sequence of images of an experiment showing bubble trapping during flow of water in a T junction of lateral size, L = 4.8 mm, Re = 980. Each image is taken every 125 μs (Movie S10). (*E*) Schematic of our experimental setup. H_2 or O_2 bubbles are generated (*Inset*) by electrolysis with an electric potential applied between a thin (75-μm) stainless steel wire and a solid electrode inside the T junction.

T junction, and ρ_f and μ are, respectively, the density and viscosity of the fluid (water). We considered mainly laminar flow conditions, focusing our study in the range $100 < Re < 1{,}000$. These inertially dominated flow conditions are common to many biological (24) and industrial flow networks. To complement the spectrum of possible situations in which bubble trapping can occur, we also performed some experiments at higher Reynolds numbers up to 5,000.

Bubbles are transported by the flow to the T junction where the unexpected trapping phenomenon occurs; indeed, the accumulation happens near a stagnation area, which is a region of expected kinematic instability. Moreover, the trapped bubbles can accumulate in time up to a saturation volume, although the bubble structures eventually disrupt and reform when the flow is unsteady for higher Reynolds numbers (see Movie S1, in which the bubble generation is switched off to show the persistence of bubble trapping). We performed flow visualization experiments to document the fluid motion, and investigated the single- and two-phase flows by performing 3D numerical simulations (see *SI Discussion* for details).

Results

Vortical Structures and Observations of Particle Trapping. By inspection of the experimental data and an analysis of the numerically simulated single-phase flow field, we determined that the mechanism that underlies the trapping phenomenon is a consequence of the vortical nature of the flow, its change with Reynolds number, and the relative motion of the suspended particles to the fluid. Specifically, two counterrotating vortices develop directly at the T junction at moderate Reynolds numbers where inertial effects become significant (Fig. 2*A*). The inertial effects combined with the abrupt change in direction create a complicated 3D flow typical of T junctions (5), similar to Dean flow in a curved pipe (25, 26). Our simulations indicate that a region of low pressure develops in these vortical structures, and consequently a localized high-pressure gradient is observed (Fig. 2*B*, *Upper*). In addition, the fluid flow is altered by the pressure gradient, and flow reversal within the vortex core can occur (Fig. 2*B*, *Lower*), which is the flow feature known as vortex breakdown (27–29), similar to the case of a vortex in a constricted tube (30). The vortex breakdown phenomenon has been studied previously for a rotating container or flow over a delta wing (31).

As will be discussed further below, on top of these vortical flow features the resulting hydrodynamic force from the fluid on the suspended particles acts in the negative pressure gradient direction and is able to drag particles relative to the fluid, which contributes to the unusual particle trajectories observed in our experiments. Detailed Euler–Lagrange simulations indicate that under these conditions bubble trapping is indeed possible, as illustrated in Fig. 2*C* (see also the simulation results displayed in Figs. S1–S7 and Movie S2). However, what is the exact mechanism that causes particle trapping immediately after the particles have entered the T junction, and for which combinations of flow and particle parameters is trapping possible?

Flow Transitions. By analysis of our single-phase flow simulations, we identified several critical Reynolds numbers where important flow transitions occur. For $Re > 50$, two counterrotating vortices develop in the channel. The typical picture of such a vortex is a spiral-like structure with flow directed along the vortex axis in the flow direction. For $Re > 220$ the axial velocity at the axis of the vortex u_x starts to decrease as an adverse pressure gradient exists within the vortical structures, i.e., the pressure is increasing in the flow direction (Fig. 3 *A* and *B*). The vortex core was identified as the location of the pressure minima in y–z cross-sections along the x axis. For $Re > 350$ we find four symmetric steady recirculation zones where the fluid speed itself reverses sign, i.e., the local pressure gradient drives the flow against the mean flow field direction, trapping pockets of fluid within the vortices, which is the signature of vortex breakdown. In Fig. 3*C* we report the axial velocity in the vortex core u_x to illustrate this flow reversal transition (flow visualization, as shown in Fig. S8, was used to validate the simulations). This shift in the pressure and velocity distributions occurs below the steady–unsteady flow transition that occurs at higher Reynolds numbers (i.e., at $Re \sim 550$). Our results suggest that such a significant flow feature—the vortex breakdown phenomenon—also occurs in a common T junction, which drives the particle-trapping phenomenon we have documented here.

Parameter Space for Trapping. We now focus on the identification of particle parameters, i.e., size and density, for which trapping is observed. First, we will consider gas bubbles, which is the limiting case of small particle–fluid density ratios $\rho = \rho_p/\rho_f$. A phase plane summarizing our experimental observations for bubble accumulation is given in Fig. 4 (and Fig. S9). For $200 < Re < 900$, corresponding to a steady or unsteady laminar flow, larger bubbles

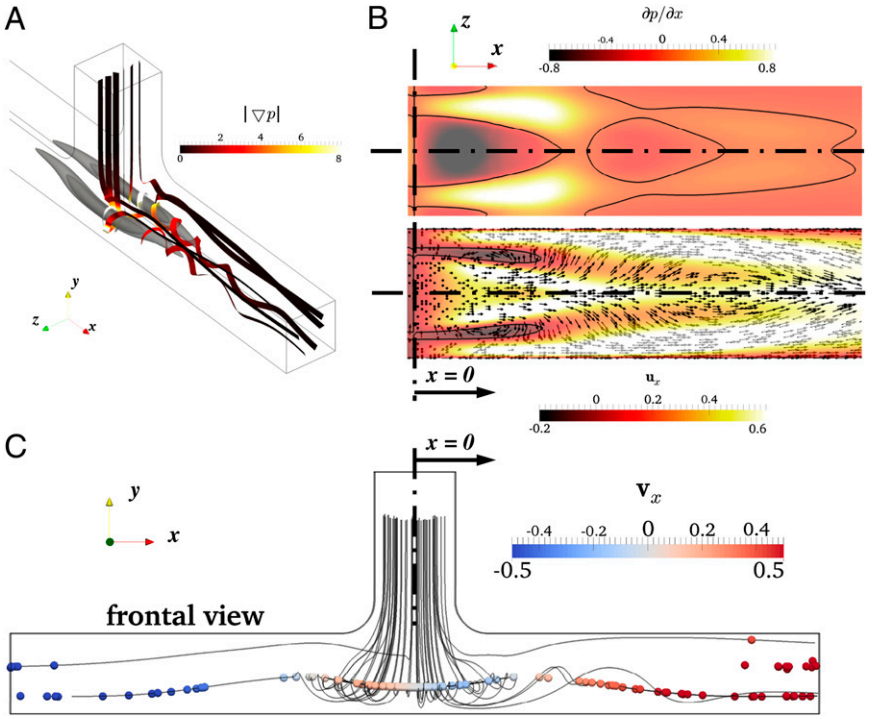

Fig. 2. Three-dimensional flow features responsible for particle trapping. (*A*) Numerical simulations at $Re = 400$ show that two symmetric vortices form at the T junction in a steady flow; streamlines are indicated and colors indicate the magnitude of the pressure gradient $|\nabla p|$. (*B*) *xz* sections at the center of the vortices ($y = 0.36$, $Re = 400$; the *y*–*z* symmetry plane at $x = 0$ and indicated by the vertical dashed-dotted line is located at the center of the inlet channel): the color contours (*Upper*) indicate the pressure gradient in the *x* direction $\partial p/\partial x$, and the lines indicate the isocontour at $\partial p/\partial x = 0$. (*Lower*) Vectors point in the direction of the fluid velocity, the color contours indicate the flow speed in the *x* direction u_x, and the line indicates the isocontour at $u_x = 0$. (*C*) Particle positions (relative particle radius $a = 0.05$, relative density $\rho_\pi/\rho_\phi = 0.15$; particles are colored according their axial velocity v_x) and pathlines 10 dimensionless time units after injection.

get trapped, but smaller bubbles are unable to reach the axis of the vortex. The smaller bubbles nonetheless remain trapped within the vortex, rotating at some distance from the core, whereas larger bubbles are trapped closer to the core (Fig. 5 *A* and *B*, as well as Movies S3–S5).

Moreover, for $Re < 900$ bigger bubbles are more sensitive to a change in the pressure drop at the outlet. We have used this effect to selectively manipulate bubbles in the vortex. For example, by slightly changing the pressure drop at one outlet we can induce drift of large trapped bubbles, thus accomplishing bubble sorting (Fig. 5*C* and Movie S6).

When air bubbles are confined inside the recirculation zones their number density is increased. This situation can lead to bubble coalescence. In the absence of surfactants, which suppress coalescence, bubbles trapped in the vortex grow by coalescing with incoming bubbles to produce a single large bubble that remains stationary at the center of the vortex core (Fig. 6*A* and Movie S7). A control experiment with a small concentration of surfactant (SDS, 0.1 g/l) in the aqueous solution highlights the case of noncoalescing bubbles (Fig. S10). Thus, trapping is not affected by coalescence, but coalescence, which leads to an increase of the mean bubble diameter in the middle of the T junction,

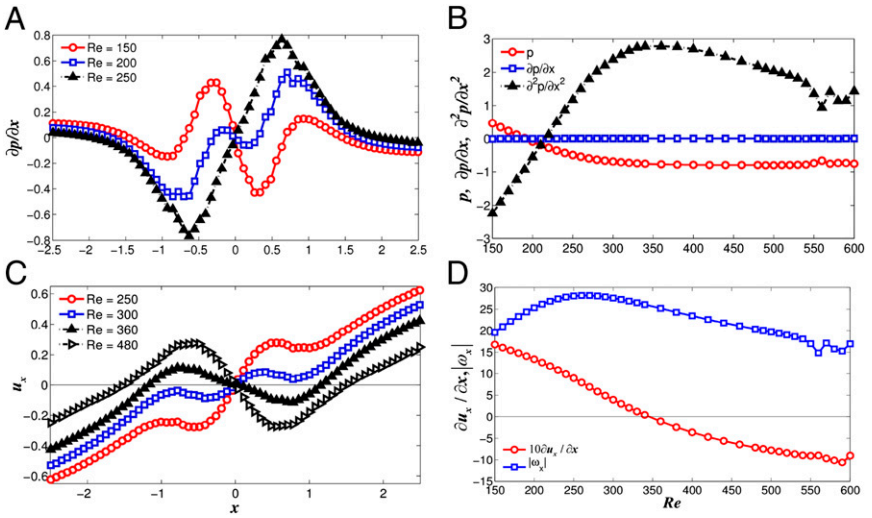

Fig. 3. Velocity and pressure distributions along the vortex core. (*A*) Axial pressure gradient versus *x* position for various Reynolds numbers, indicating a shift in the second derivative of the pressure profile between $Re = 200$ and $Re = 250$ (note that $x = 0$ is located at the center of the inlet channel). (*B*) Pressure and its spatial derivatives versus the Reynolds number ($x = 0$; for $Re > 210$, $\partial^2 p/\partial x^2$ changes sign). (*C*) Axial fluid velocity at the vortex core versus *x* position for various Reynolds numbers, indicating a change in the axial velocity gradient between $Re = 300$ and $Re = 360$. (*D*) Axial velocity gradient $\partial u_x/\partial x$ and axial component of the vorticity versus the Reynolds number ($x = 0$; for $Re > 350$, $\partial u_x/\partial x$ changes sign).

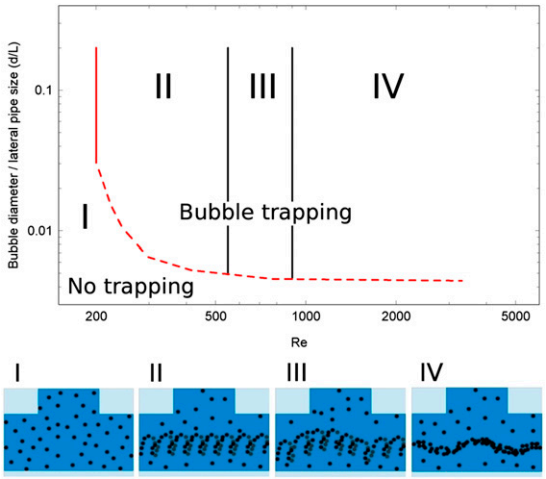

Fig. 4. Phase plane of bubble behavior based on experimental data. In the graph the size of the bubbles trapped in the vortices is plotted versus *Re*. Four regions are identified: (I) $Re < 200$: no bubble trapping. (II) $200 < Re < 550$: larger bubbles get trapped in the center of the vortices whereas smaller bubbles stay at a distance from the cores and continually rotate. The flow is time independent. (III) $550 < Re < 900$: bubbles are trapped as in II but the flow is unsteady. (IV) $Re > 900$: bubbles are trapped and form chain-like structures. See also Fig. S9.

will even increase the consequences of the trapping. This eventuality should be considered when designing an industrial piping system (e.g., a heat exchanger) where no air pockets are allowed to form. In fact, the trapping mechanism that we are describing can lead to the accumulation and, eventually, size increase due to coalescence of small air bubbles present in the pipeline. Therefore, the results we are presenting can be used to avoid flow conditions (i.e., Reynolds number) or geometries that could pose such a safety risk.

We also performed experiments dispersing low-density solid particles (hollow glass, density $\rho_p = 0.15$ g/cm^3, average diameter 60 μm), which are used in industrial processes (2, 3). Thus, we confirmed the generality of the trapping phenomenon that occurs for solid particles in the same way as for the bubbles (Fig. 6*B* and Movie S8). Finally, we demonstrated that pulsatile flow conditions similar to physiological flows also lead to the trapping of low-density material (Fig. 6*C* and Movie S9): at each 1-Hz pulse we were able to trap bubbles (coalescence was suppressed by addition of surfactants).

Next, we describe Euler–Lagrange numerical simulations that were used to reconstruct the trapping, and to help in the identification of the trapping mechanism. In these simulations we injected several hundred low-density particles (with a density ratio of 0.15) at the inlet of the T junction, and computed their trajectories using Newton's equation of motion. Fluid–particle force models valid for the ranges of Reynolds number of our experiments were used in these simulations (see *SI Discussion* for details). Our simulations confirmed the experimental results, i.e., they show that whereas small particles cannot enter the vortex, large low-density particles rapidly move toward the vortex core and become trapped. Furthermore, the simulations reveal a subtle detail of the trapping process: depending on the axial pressure gradient and flow velocity, big particles get trapped only temporarily at $Re < 300$, whereas for $Re > 350$ permanent trapping is observed. In the next section we explain the origin for this effect of particle size in the discussion of the theoretical model we developed.

Trapping Mechanism. Our flow experiments were conducted in small channels, where the Reynolds number is large so the flow is dominated by inertia, and buoyancy effects are small, i.e., $gL/U^2 << 1$. Consequently, gravity does not play a role as it does for the well-known bubble accumulation in Couette–Taylor flows (32). Instead, the trapping of particles we observe combines the phenomenon of bubble (pressure-gradient-induced) movement toward the center of vortices as observed in turbulent flows (17–19, 33–35) with the vortex breakdown phenomenon in the T junction described in Figs. 2 and 3. As already mentioned, the pressure distribution plays a critical role for this scenario, which is also the case for the well-known accumulation of bubbles in the vortex structures of a turbulent flow (17–19). However, the key difference is that in these previous observations of bubble trapping, effects due to gravity (i.e., a hydrostatic pressure gradient and the resulting bubble rise velocity) were needed to explain the trapping or exit of bubbles from a vortex. This led to the conclusion that bubbles with small rise velocity (i.e., small particles or low gravity) always become trapped in a vortex. As we will show below, trapping in the vortex structure that forms at a T junction cannot occur for small particles, and does not require the inclusion of gravitational effects.

As the trapping phenomenon we investigate occurs under laminar flow conditions, but at nonzero Reynolds numbers, one might seek an explanation for the bubble trapping in the area of inertial microfluidics (36). Literature in this field suggests that either (*i*) secondary flows, e.g., Dean-like flow structures (25, 26) or vortex formation, (*ii*) lift forces, or (*iii*) a combination of both effects might be responsible for particle migration, and consequently a change in the particles' trajectories, e.g., ref. 7. However, our simulations clearly show that lift forces have only an insignificant effect on the particle trajectories in our flow setup and for the Reynolds number range we study.

A key feature of a trap is that it allows particles (or bubbles) to enter a region, while it is impossible for particles to exit. Thus, we need to answer two questions: (*i*) Which parameters, i.e., particle properties and flow features, lead to particle entrainment into the vortex? and (*ii*) Which parameters lead to the exiting of particles from the vortex? The answers to these questions are nontrivial due to the complex hydrodynamic interactions of particles in swirling flows (17, 37–39). Using force models as well

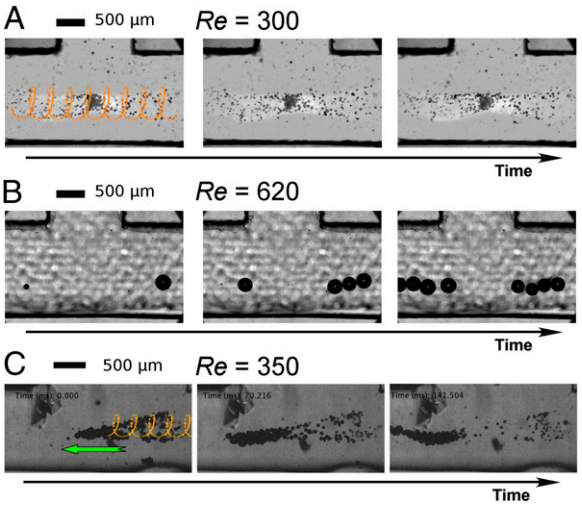

Fig. 5. Effect of bubble size and the bubble sorting mechanism. Time sequences that document the different behavior of air bubbles in the experiments. For $Re < 900$ (*A*) small bubbles are trapped but maintain a distance from the vortex core and rotate around it, whereas (*B*) bigger bubbles get trapped directly at the core. As a consequence (*C*) it is possible to selectively sort bubbles depending on their size. By changing the pressure at one outlet it is possible to move bigger bubbles toward this direction as the bigger bubbles are more sensitive to a change in pressure than the smaller bubbles (Movie S6). The background of the images *A* has been removed to enhance the contrast.

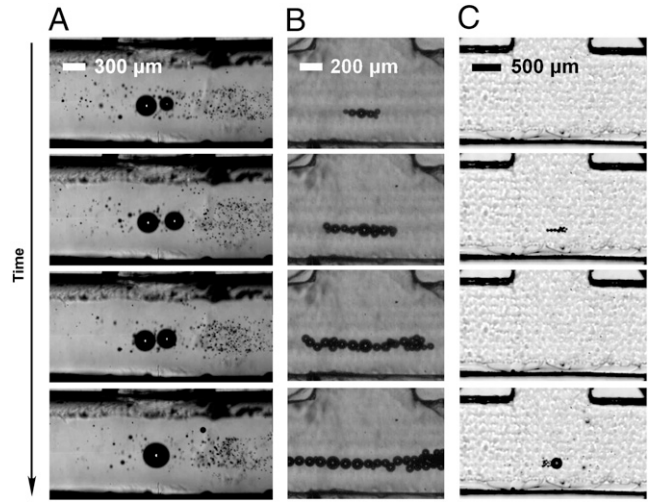

Fig. 6. Generalization: bubble growth, trapping of solid particles and the influence of pulsatility. Time sequence images for Re = 500. (*A*) Bubbles accumulate at a T junction and, in the absence of surfactants, can coalesce and grow. (*B*) Trapping of solid particles: hollow glass beads (ρ_P = 0.15 g/cm^3) accumulate at the T junction. (*C*) Bubble trapping in a pulsed flow (in these images and in Movie S9 the frequency is 1 Hz). At each pulse the flow can trap air bubbles.

as simulations, we provide detailed understanding of the trapping phenomenon; further details are provided in *SI Discussion*.

We use a force balance based on Newton's equation of motion in the main flow (x) direction to define a critical particle radius a^*_{ax}, which characterizes axial entrainment or exit of particles (the asterisk indicates a dimensional variable in contrast with the dimensionless variables we will introduce later). The critical condition is that the particle is arrested at a certain axial position, i.e., that its axial velocity is zero. This force balance is based solely on the fluid pressure gradient force $F^*_{\nabla p} = -4\pi/3\ a^{*3}_{ax}\ \nabla p^*$, and the fluid–particle drag force $F^*_{drag} = 6\pi a^*_{ax}\mu\ u^*_x\ f(Re_p)$ acting on an isolated particle. Here u^*_x and p^* are the axial (i.e., x-) component of the fluid velocity and the local pressure at the particle location, respectively. The function $f(Re_p)$ captures the dependency of the drag force (we use the Schiller–Nauman model, which is simple and suits our application; see ref. 40) on the particle Reynolds number, $Re_p = 2a^*_{ax}\ u^*_x\rho_f/\mu$. Similarly, a force balance in the radial direction is used to define a critical particle radius a^*_{rad}, which indicates whether particles will leave or enter the vortex in the radial direction. This force balance, however, must include a centrifugal force $F^*_c = 4\pi/3a^{*3}_{ax}\rho_p\ u^{*2}_\phi/r^*$ acting on the particle, where u^*_ϕ is the fluid velocity in the tangential direction. Our Euler–Lagrange simulations indicated that lift forces are typically an order of magnitude smaller than drag and pressure gradient forces. Hence, these forces were not included in our analysis (see *SI Discussion* for details and the assumptions used to establish the force balances).

It is now convenient to write these two force balances in nondimensional form using U as the reference velocity, L as the reference length, and $\rho_f U^2$ as the reference pressure. This yields two relationships for the (dimensionless) critical particle radii a_{ax} and a_{rad}:

$$0 = 6\pi a_{ax} u_x f(Re_p) - Re\frac{4\pi}{3}a^3_{ax}\frac{\partial p}{\partial x}, \qquad [1]$$

$$0 = 6\pi a_{rad} u_r f(Re_p) - Re\frac{4\pi}{3}a^3_{rad}\left(\frac{\partial p}{\partial r} - \frac{\rho_p}{\rho_f}\frac{u^2_\phi}{r}\right). \qquad [2]$$

Here u_x, u_r, u_ϕ, and p are the local dimensionless fluid velocities in the mean flow, radial, and tangential directions, as well as the local pressure, respectively. These quantities have been extracted from our single-phase flow simulation data. Furthermore, the particle Reynolds number now reads $Re_p = 2a\ Re\ u_{rel}$, with u_{rel} being the dimensionless fluid–particle velocity, corresponding to either the axial or radial fluid velocity, in the case of the axial or radial force balance, respectively. This relationship indicates that Re_p is much smaller than the channel Reynolds number Re, a fact that has important implications for the relevance of other forces as discussed in *SI Discussion*.

We solve the above relationships iteratively to construct 2D maps of a_{ax} and a_{rad} in cross-sections normal to the mean flow (i.e., x-) direction (*SI Discussion*). These maps indicate that particles with a radius larger than (the locally defined) critical radii a_{ax} or a_{rad} will be entrained due to the action of pressure gradient forces, whereas smaller particles must exit the vortex due to fluid–particle drag forces.

In summary, our theoretical model indicates that low-density particles always enter the vortex radially due to the radial pressure distribution, i.e., $a_{rad} << 1$ for $\rho_p/\rho_f < 1$. This tendency for radial entrainment is already present at Reynolds numbers as low as $Re \sim 100$, which is just after the vortices are formed at the T junction and much before trapping is observed. However, particles (independent of their density; see Eq. **1**) will exit the vortex in the axial direction for Re smaller than *ca.* 200, depending on the particle size. The situation is very different for particles with a density ratio of $O(1)$ or higher: these particles can enter the vortex axially (in the case axial backflow in the vortex core is observed) or radially (in case u_r is negative), but must exit the vortex in the radial direction because of centrifugal forces. Our model computations show that the critical density ratio for the radial trapping is *ca.* $\rho_{crit} \sim 0.7$, which, in a first approximation, is independent of the Reynolds number. In summary, our theoretical analysis explains the trapping mechanism by the formation of surprisingly high local pressure gradients, and the subsequent hydrodynamic forces, which, when combined with vortex breakdown at the T junction, lead to particle accumulation in this region. Despite its simplicity, our analysis is able to predict the experimentally observed axial and radial positions of particle accumulation surprisingly well (see *SI Discussion* for details).

Discussion

The experiments and analyses we presented here identify a heretofore unrecognized mechanism of particle trapping in common flows. This trapping is the result of the formation of an adverse pressure gradient and backflow in the core of two vortices that form directly at the T junction. Low-density dispersed material with density of less than ~0.7 times the continuous phase density will get trapped in vortices when the flow Reynolds number is larger than about 200 (see *SI Discussion* for more details). This phenomenon is even observed when the flow becomes unsteady, as we have observed experimentally trapping up to Re = 5,000, or in case of a pulsating flow. In case the accumulation of material is undesirable or even dangerous, e.g., as is the case for gas embolism, our data can be used to choose suitable flow parameters. The trapping mechanism may also prove useful for the design of new separation equipment, such as devices for size classification of low-density particles, debubbling devices, or microfluidic flotation devices.

Materials and Methods

We realized the T-junction devices by casting polydimethylsiloxane (PDMS, Sylgard 184 silicone elastomer kit, Dow Corning) on a T-shaped plastic mold obtained by 3D printing (for the devices with L = 0.4, 0.4, 1.2, 1.5 mm) or by machining (for the device with L = 4.8 mm). Once cured (after 1 h at 70 °C), we removed the solidified PDMS from the mold, punched inlet and outlet holes, and sealed the device on a glass slide (41). We then connected the smaller devices to a programmable syringe pump (Harvard Apparatus Ultra)

or the larger device ($L = 4.8$ mm) to a centrifugal pump (ViaAQUA 3000). We flow a solution of deionized water and sodium sulfate (Na_2SO_4, ~1 g/l) through the channel; the added salt is necessary for the controlled generation of bubbles by electrolysis between a thin (75 μm) stainless steel wire and a solid electrode; Fig. 1*D*. Depending on the flow velocity, the diameter of the bubbles varied between 20 and 500 μm. We performed experiments with low-density solid particles using hollow glass spheres (Mo-sci Specialty Products, LLC), with a density $\rho_p = 0.15$ g/cm^3 and an average diameter of 60 μm. We note that dispersing these particles in the fluid permitted easier accumulation compared with bubbles (and so better visualization) only because the bubble generation method we used provides only a few big bubbles, with the majority of bubbles comparable in size to the electrolysis wire (~100 μm). An experiment performed in a bigger device ($L = 4.8$ mm), where bubbles are created by incorporating air by strongly stirring a mixture of water and glycerol, shows the same behavior of the solid beads (Fig. 1*E* and Movie S10). We recorded high-speed videos via a Vision Research Phantom v7.3 camera at a frame rate up to 35,000 frames per second.

Single-phase fluid flow in the T junction was simulated using a finite-volume Navier–Stokes solver on unstructured meshes. The open-source package OpenFOAM (42) was used as the simulation software with appropriate, second-order accurate, discretization schemes in space and time. The grid resolution effects were kept under control by performing simulations with different spatial grid resolutions. The dimensionless distance $y^+ = y_f\sqrt{\tau_w\rho_f}/\mu$ to the first grid cell near the wall was checked, and a grid was chosen such that $y^+ < 0.5$. Here y_f is the normal distance between the centroid of the first grid cell and the wall, and τ_w is the magnitude of the wall shear stress evaluated from the velocity gradient normal to the wall and the viscosity μ. The time step was controlled to ensure a maximum Courant number of $Co < 0.3$ (more details regarding resolution requirements are summarized in *SI Discussion*). Data on the local pressure and velocity distribution have been resampled (using MATLAB) on a regular grid to identify the vortex core, and to calculate the flow variables in the vortex core, as well as the entrainment and exit parameters. The Euler–Lagrange simulations were performed using a modified version of the code CFDEM (www.cfdem.com). In these simulations the details of the flow around individual particles were not resolved, and simulations were performed in "one-way" coupling mode, i.e., particles were passive tracers and did not influence fluid flow. The force models used include fluid–particle drag (43), lift (44), as well as forces due to the local pressure gradient and viscous stresses.

ACKNOWLEDGMENTS. We thank François Gallaire, Ian Griffiths, and Kevin K. Chen for helpful conversations and suggestions.

1. Meng H, et al. (2007) Complex hemodynamics at the apex of an arterial bifurcation induces vascular remodeling resembling cerebral aneurysm initiation. *Stroke* 38(6): 1924–1931.
2. McDonald CJ, Devon MJ (2002) Hollow latex particles: Synthesis and applications. *Adv Colloid Interface Sci* 99(3):181–213.
3. Seymour RB (1976) The role of fillers and reinforcements in plastics technology. *Polym-Plast Technol Eng* 7(1):49–79.
4. Wong S, Ward M, Wharton C (2004) Micro T-mixer as a rapid mixing micromixer. *Sens Actuators B Chem* 100(3):359–379.
5. Haller D, Woias P, Kockmann N (2009) Simulation and experimental investigation of pressure loss and heat transfer in microchannel networks containing bends and T-junctions. *Int J Heat Mass Transfer* 52(11):2678–2689.
6. Link DR, Anna SL, Weitz DA, Stone HA (2004) Geometrically mediated breakup of drops in microfluidic devices. *Phys Rev Lett* 92(5):054503.
7. Wang X, Zhou J, Papautsky I (2013) Vortex-aided inertial microfluidic device for continuous particle separation with high size-selectivity, efficiency, and purity. *Biomicrofluidics* 7(4):44119.
8. Bhagat AAS, Kuntaegowdanahalli SS, Papautsky I (2008) Inertial microfluidics for continuous particle filtration and extraction. *Microfluidics Nanofluidics* 7(2):217.
9. Lenshof A, Laurell T (2010) Continuous separation of cells and particles in microfluidic systems. *Chem Soc Rev* 39(3):1203–1217.
10. PARC-A Xerox Company Low-energy, compact, cost-effective separation for drinking water and wastewater treatment along with precious resource recovery. Available at www.parc.com/services/focus-area/clean-water. Accessed October 2013.
11. Muth CM, Shank ES (2000) Gas embolism. *N Engl J Med* 342(7):476–482.
12. Bass RM, Longmore DB (1969) Cerebral damage during open heart surgery. *Nature* 222(5188):30–33.
13. Bull JL (2005) Cardiovascular bubble dynamics. *Crit Rev Biomed Eng* 33(4):299–346.
14. Lindner JR (2004) Microbubbles in medical imaging: Current applications and future directions. *Nat Rev Drug Discov* 3(6):527–532.
15. Mei R (1996) Velocity fidelity of flow tracer particles. *Exp Fluids* 22(1):1–13.
16. Vigolo D, Griffiths IM, Radl S, Stone HA (2013) An experimental and theoretical investigation of particle–wall impacts in a T-junction. *J Fluid Mech* 727:236–255.
17. Magnaudet J, Eames I (2000) The motion of high-Reynolds-number bubbles in inhomogeneous flows. *Annu Rev Fluid Mech* 32:659–708.
18. Balachandar S, Eaton JK (2010) Turbulent dispersed multiphase flow. *Annu Rev Fluid Mech* 42:111–133.
19. Mazzitelli IM, Lohse D, Toschi F (2003) On the relevance of the lift force in bubbly turbulence. *J Fluid Mech* 488:283–313.
20. Milenkovic RZ, Sigg B, Yadigaroglu G (2007) Bubble clustering and trapping in large vortices. Part 1: Triggered bubbly jets investigated by phase-averaging. *Int J Multiphase Flow* 33(10):1088–1110.
21. Husain HS, Hussain F, Goldshtik M (1995) Anomalous separation of homogeneous particle-fluid mixtures: Further observations. *Phys Rev E Stat Phys Plasmas Fluids Relat Interdiscip Topics* 52(5):4909–4923.
22. Goldshtik M, Husain HS, Hussain F (1992) Loss of homogeneity in a suspension by kinematic action. *Nature* 357:141–142.
23. Shinbrot T, Alvarez MM, Zalc JM, Muzzio FJ (2001) Attraction of minute particles to invariant regions of volume preserving flows by transients. *Phys Rev Lett* 86(7): 1207–1210.
24. Takeuchi S, Karino T (2010) Flow patterns and distributions of fluid velocity and wall shear stress in the human internal carotid and middle cerebral arteries. *World Neurosurg* 73(3):174–185, discussion e27.
25. Dean WR (1927) Note on the motion of fluid in a curved pipe. *Philos Mag Series* 7:208–223.
26. Dean WR (1928) The stream-line motion of fluid in a curved pipe. *Philos Mag Series* 7:673–695.
27. Benjamin TB (1962) Theory of the vortex breakdown phenomenon. *J Fluid Mech* 14:593–629.
28. Leibovich S (1978) The structure of vortex breakdown. *Annu Rev Fluid Mech* 10:221–246.
29. Shtern V, Hussain F (1999) Collapse, symmetry breaking, and hysteresis in swirling flows. *Annu Rev Fluid Mech* 31:537–566.
30. Lopez JM (1994) On the bifurcation structure of axisymmetric vortex breakdown in a constricted pipe. *Phys Fluids* 6(11):3683–3693.
31. Hall MG (1972) Vortex breakdown. *Annu Rev Fluid Mech* 4:195–218.
32. Climent E, Simonnet M, Magnaudet J (2007) Preferential accumulation of bubbles in Couette-Taylor flow patterns. *Phys Fluids* 19(8):083301.
33. Calzavarini E, Cencini M, Lohse D, Toschi F; International Collaboration for Turbulence Research (2008) Quantifying turbulence-induced segregation of inertial particles. *Phys Rev Lett* 101(8):084504.
34. Biferale L, Boffetta G, Celani A, Lanotte A, Toschi F (2005) Particle trapping in three-dimensional fully developed turbulence. *Phys Fluids* 17(2):021701.
35. Toschi F, Bodenschatz E (2009) Lagrangian properties of particles in turbulence. *Annu Rev Fluid Mech* 41:375–404.
36. Di Carlo D (2009) Inertial microfluidics. *Lab Chip* 9(21):3038–3046.
37. Brennen CE (2005) *Fundamentals of Multiphase Flows* (Cambridge Univ Press, Cambridge, UK).
38. van Nierop EA, et al. (2007) Drag and lift forces on bubbles in a rotating flow. *J Fluid Mech* 571:439–454.
39. Bluemink JJ, Lohse D, Prosperetti A, Van Wijngaarden L (2009) Drag and lift forces on particles in a rotating flow. *J Fluid Mech* 643:1–31.
40. Crowe CT, Michaelides EE (2005) Basic Concepts and Definitions. *Multiphase Flow Handbook*, ed Crowe CT (CRC, Boca Raton, FL).
41. Duffy DC, McDonald JC, Schueller OJA, Whitesides GM (1998) Rapid prototyping of microfluidic systems in poly(dimethylsiloxane). *Anal Chem* 70(23):4974–4984.
42. The OpenFOAM Foundation OpenFOAM 2.1.x, www.openfoam.org.
43. Beetstra R, Van Der Hoef MA, Kuipers JAM (2007) Drag force of intermediate Reynolds number flow past mono- and bidisperse arrays of spheres. *AIChE J* 53(2): 489–501.
44. Kurose R, Komori S (1999) Drag and lift forces on a rotating sphere in a linear shear flow. *J Fluid Mech* 384:183–206.